Microsc. Microanal. Page 1 of 12
doi:10.1017/S1431927611000456

Microscopy AND Microanalysis

© MICROSCOPY SOCIETY OF AMERICA 2011

An Open-Source Engine for the Processing of Electron Backscatter Patterns: EBSD-Image

Philippe T. Pinard,[1,*] Marin Lagacé,[2] Pierre Hovington,[2] Denis Thibault,[2] and Raynald Gauvin[1]

[1]*Materials and Mining Engineering Department, McGill University, 3610 University Street, Montreal, Quebec H3A 2B2, Canada*
[2]*Materials Science Department, Institut de recherche d'Hydro-Québec, 1800 Lionel-Boulet Boulevard, Varennes, Québec J3Z 1S1, Canada*

Abstract: An open source software package dedicated to processing stored electron backscatter patterns is presented. The package gives users full control over the type and order of operations that are performed on electron backscatter diffraction (EBSD) patterns as well as the results obtained. The current version of EBSD-Image (www.ebsd-image.org) offers a flexible and structured interface to calculate various quality metrics over large datasets. It includes unique features such as practical file formats for storing diffraction patterns and analysis results, stitching of mappings with automatic reorganization of their diffraction patterns, and routines for processing data on a distributed computer grid. Implementations of the algorithms used in the software are described and benchmarked using simulated diffraction patterns. Using those simulated EBSD patterns, the detection of Kikuchi bands in EBSD-Image was found to be comparable to commercially available EBSD systems. In addition, 24 quality metrics were evaluated based on the ability to assess the level of deformation in two samples (copper and iron) deformed using 220 grit SiC grinding paper. Fourteen metrics were able to properly measure the deformation gradient of the samples.

Key words: EBSD, post-processing, EBSP, image quality, image analysis, deformation

Introduction

Several third-party software programs exist for post-processing electron backscatter diffraction (EBSD) mappings using the different output files of commercial software: VMAP (Humphreys, 2004), MTEX (Hielscher & Schaeben, 2008), and open-ebsd (http://code.google.com/p/open-ebsd). To our knowledge, no freely available software is available for processing electron backscatter diffraction patterns (EBSP). As such, an open-source, cross-platform EBSD software, entitled EBSD-Image, was developed to offer a flexible and expandable interface, allowing the implementation of any algorithm related to the analysis of stored diffraction patterns (e.g., quality metrics). The software was developed to serve as a research and developmental tool for the EBSD community. Its main objective is to give a high level of flexibility to the user instead of targeting a high processing speed.

The primary use of EBSPs is to perform phase identification and orientation measurements. In these applications, the angles between Kikuchi bands and, on some occasions, the width of the bands are used (Wright, 1992; Krieger Lassen, 1994). It is also possible to extract a large amount of information from a diffraction pattern by looking at the variation in its "quality". From an EBSD point of view, "quality" is a parameter that quantifies the crystallographic uniformity within the interaction volume. Different features of a diffraction pattern may be used to assess its quality: intensity, contrast, sharpness, noise level, etc.—quality metrics can be designed to highlight these features for each diffraction pattern in a mapping.

Quality metrics have been used for different applications: to discriminate between crystallographically similar phases, e.g., ferrite and martensite (Wu et al., 2005; Ryde, 2006; Petrov et al., 2007); to estimate the accuracy of the orientation measurements; and to establish a better clean-up procedure (Hovington et al., 2009). This work focuses on evaluating how well quality metrics are able to assess the level of deformation inside a sample. When a crystal lattice is plastically deformed, the dimensions of its lattice are distorted: this nonuniformity leads to a greater distribution of the diffraction angles. The deformation is manifested by a decrease in sharpness of the edges of the Kikuchi bands (Wilkinson & Dingley, 1991; Keller et al., 2004). Wright and Nowell (2006) have shown that the image quality metric, as calculated by the TSL OIM software (AMETEK, Inc., Berwyn, PA, USA), can be used to evaluate deformation.

Quality metrics found in the literature as well as new ones devised by the authors were evaluated using EBSD-Image: this was done by measuring the depth of the deformation induced by grinding copper and iron samples with 220 grit SiC paper. The compression loading and raking action of the SiC particles create a deformation gradient starting from the surface of the sample inward. Prior to this evaluation, a description of EBSD-Image will be given, highlighting the structure of the software, the implementation of its strategic algorithms, its file formats, and the tools developed to analyze large datasets. Finally, simulated dif-

Received July 30, 2010; accepted March 24, 2011
*Corresponding author. E-mail: philippe.pinard@mail.mcgill.ca

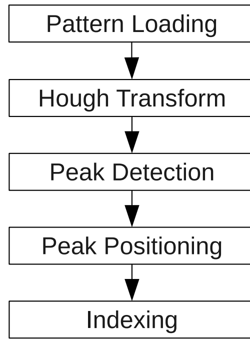

Figure 1. Structure of the analysis engine.

fraction patterns based on kinematic theory were used as a benchmark for the algorithms implemented in the software to better understand the results obtained using the tested quality metrics.

Description of the Software

Platform

Many of the algorithms involved in processing EBSPs as well as the post-treatment and analysis of EBSD mappings are directly derived from image analysis routines. This includes standard operations such as erosion, dilation, convolution, thresholding, etc., and more advanced ones such as the Hough and Fourier transform. It is for this reason that EBSD-Image is built on top of the image analysis software, RML-Image (www.rmlimage.com): the users have access to image analysis algorithms to analyze their results and extract additional information. This contrasts with other EBSD software, which are more focused on EBSD specific operations.

Structure

For each diffraction pattern in an EBSD mapping, processing consists of performing a series of operations on that EBSP and extracting some result. The difference with EBSD-Image lies in the flexibility given to the user, who can choose which operations to perform and which results to extract. An operation is defined as any process of taking one or more inputs and returning one or more outputs. The engine has a specific structure, organizing operations into five distinct steps (Fig. 1). Examples of algorithms within these steps will be discussed in the next section.

Logically, the first step of an operation is to load into memory the diffraction pattern as an 8-bit grayscale image. It also involves enhancement algorithms to improve the quality and reduce the noise in the pattern (e.g., median filter), as well as the selection of a region of interest in the pattern to ignore noisy edges. The second step is related to the Hough transform, which transforms the pattern's image space into the Hough space. Kikuchi bands inside the pattern are visible as peaks in the Hough space and are more easily detected by a computer algorithm (Krieger Lassen, 1994). Different implementations of the Hough transform can be chosen or a new algorithm can be written. Third, the peaks in the Hough image must be located. Enhancement algorithms, such as a butterfly mask, can be used to facilitate peak detection (Krieger Lassen, 1994). Ultimately, a thresholding operation is performed to create a binary map where pixels may only have values of 0 and 1. In the binary map, the position (θ, ρ) and intensity of each peak can be measured. This fourth step is the "peak positioning" step. Any operation to clear unwanted peaks or to look for specific peaks may be performed as part of this step. The most intense peaks are found and used to evaluate the diffraction quality of a pattern.

Peak detection and peak positioning are separate because they are independent tasks with different objectives. Detection aims to find as many peaks as possible in the Hough space without detecting false peaks, whereas positioning precisely locates the center of each detected peak. The separation of these steps also allows intermediate operations to be performed.

The structure includes a fifth step to index EBSPs based on the identified peaks, but no algorithm is currently fully implemented. However, the tools included in EBSD-Image facilitate the implementation of such algorithms. For instance, phases can be defined manually in the graphical interface by specifying their space groups and atom positions, or by importing this information from a crystallographic information file. Routines to calculate reflectors (diffracting crystallographic planes) based on atomic scattering factors are available.

Furthermore, different mathematical representations of rotation in three-dimensional space (matrix, quaternion, Euler angles, axis angles) are implemented to perform operations on the orientation found by the indexing algorithm (e.g., to eliminate symmetrically equivalent orientations). Algorithms linking peak positions to reflectors of a given phase, such as the ones invented by Krieger Lassen (1994) and Wright (1992), could therefore be one collaborative project of the EBSD community resulting from this work.

It is important to note that the source code of EBSD-Image is structured, extensible, and documented so users can easily incorporate custom algorithms. We refer the reader to the developer's manual (www.ebsd-image.org) to obtain a complete guide of how to implement new algorithms. The manual gives additional detail of the analysis engine's structure and programming conventions.

EBSD-Image offers a simple but powerful graphical interface. A wizard (Fig. 2) guides the user through the set-up of all parameters and operations. The parameters (accelerating voltage, size of the mapping to analyze, calibration, etc.) are defined in the first few panels. The next panels are to set-up the operations, one panel per main step. Each panel has the same appearance: with available operations listed on the right and selected operations on the left. Operations developed by the user automatically appear in the available operations' list. The last step of the wizard is to decide how the experiment will be run. The preview mode allows the user to check that all operations have been performed correctly on one diffraction pattern. Another

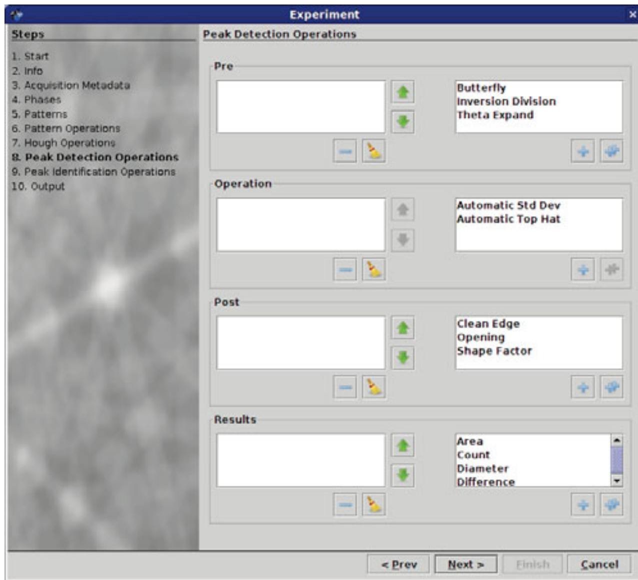

Figure 2. Screenshot of the wizard to select the operations of an experiment of EBSD-Image.

output option is to save the experiment parameters and operations to a file and relaunch the experiment at a later time. The last option runs the experiment directly on the desktop; the user can visually track the progress by selecting one of the result images.

Implementation

The implementation of the Hough transform follows the one described by Krieger Lassen (1994). To prevent biasing effects as reported by Tao and Eades (2005), the intensity at each coordinate θ and ρ in the Hough space is equal to the average (instead of the sum as originally described by Krieger Lassen) intensity of all the sinusoidal functions passing through this coordinate. The intensity of a coordinate in the Hough space is therefore the average intensity of the pixels along its corresponding line in the image space. To be represented as an image, the Hough space is quantized by two resolutions: $\Delta\theta$ and $\Delta\rho$. The choice of each resolution determines the computation time of the Hough transform, the dimensions of the Hough space image, and consequently the dimensions of the Hough peaks.

A common pattern recognition method used to increase the contrast of the peaks with respect to the background is to perform a convolution between a mask (e.g., "butterfly mask") that matches the shape of the peaks in the Hough space. To obtain a good match, the mask must have the same shape and size as the peaks. As demonstrated by Krieger Lassen (1994), both vary based on the width of a Kikuchi band and position of its peak in Hough space as well as the selected resolutions. Assuming a square convolution mask, $\Delta\theta$ and $\Delta\rho$ should be selected to obtain peaks with an aspect ratio close to unity for typical widths of Kikuchi bands and for a large portion of the Hough space. We found it intuitive to ask the user to specify the $\Delta\theta$ and calculate the resultant $\Delta\rho$, as the execution time is proportional to the former. Furthermore, the size of the mask should match the size of the peaks based on the selected resolutions.

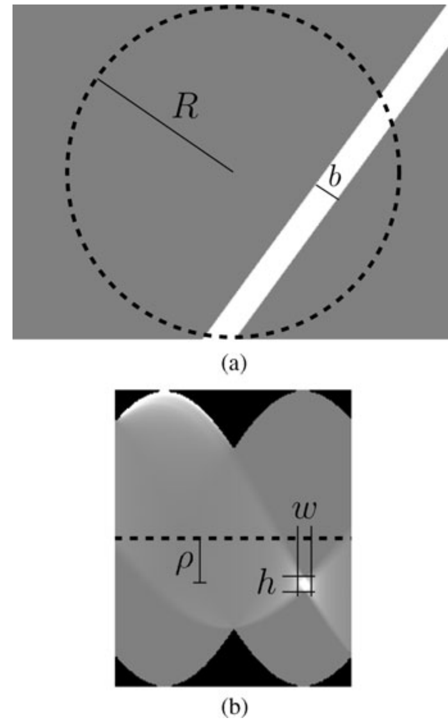

Figure 3. Example of (**a**) a simulated diffraction pattern and (**b**) the resultant Hough space used to calculate the influence of the Hough peaks' position on their aspect ratio.

To analyze the influence of peak position in the Hough space on the aspect ratio, simulated diffraction patterns (rectangular patterns, 672×512 pixels) containing only one Kikuchi band (width b of 40 pixels) were used (Fig. 3a). The slopes and positions of the simulated Kikuchi bands covered the whole Hough space. The Hough transform was performed using a $\Delta\theta$ resolution of 1°/pixel and a $\Delta\rho$ resolution of 1 pixel/pixel (Fig. 3b). Finally, the single peak in Hough space was thresholded and its dimensions were used to calculate the aspect ratio (height h/width w). To visualize the variation in aspect ratio, values were color-coded and plotted as a function of the peak position in the Hough space (Fig. 4a). In Figure 4b, using the same color scale, the analysis was repeated using a circular pattern (radius R of 256 pixel) for the region of interest. The aspect ratio using a circular mask (Fig. 4b) has a much more uniform distribution as a function of θ than the one calculated without a mask (Fig. 4a). The comparison of these two figures illustrates the importance of selecting a circular region of interest from rectangular patterns to eliminate the variation of aspect ratio as a function of θ. This variation can be explained by the different possible band lengths in the diffraction pattern. Oblique bands crossing the center of a rectangular diffraction pattern are longer than horizontal or vertical bands crossing the center or those near the edges. This effect is removed by using a circular pattern: the maximum length of the bands is determined by the diam-

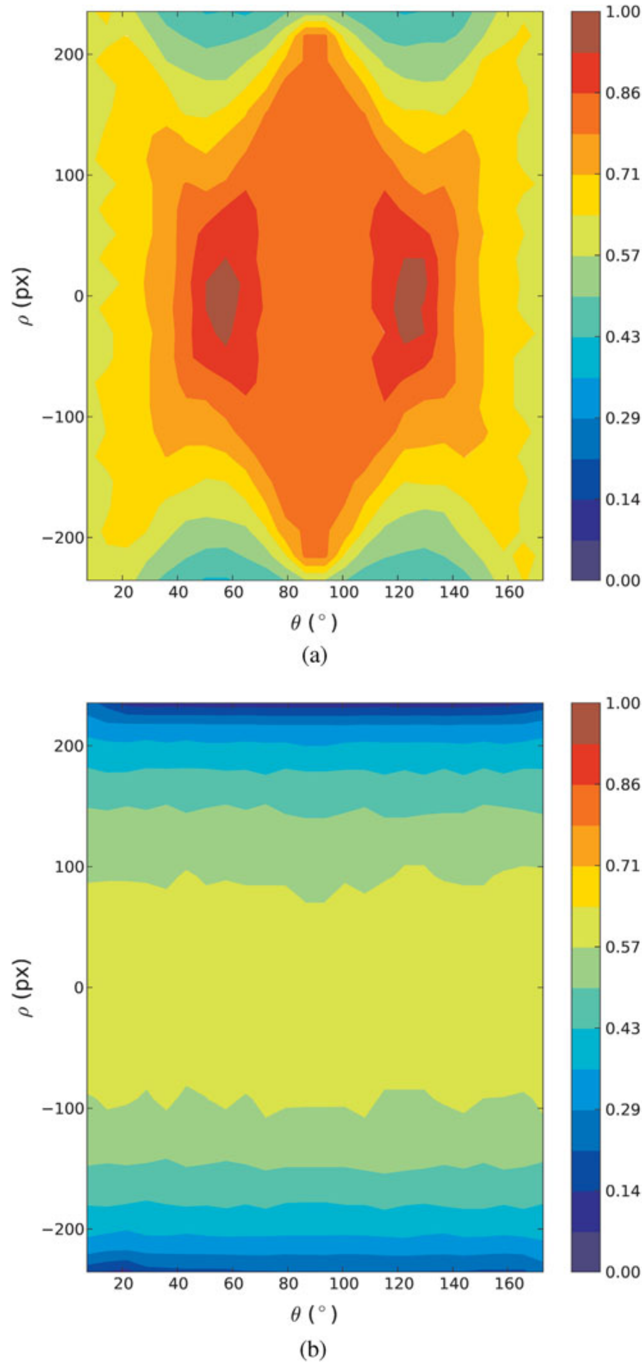

Figure 4. Variation of the aspect ratio for the peaks in Hough space (**a**) for a rectangular diffraction pattern (672 × 512 pixels) and (**b**) for a circular diffraction pattern (radius of 256 pixels). The color bar represents the normalized variation of the aspect ratio for both cases.

eter of the pattern. The variation as a function of ρ is due to a decrease in the length of the bands as they are located further away from the center of the pattern. These results highlight the importance of the circular mask.

Krieger Lassen (1994) derived two equations to express the height and width of peaks in Hough space for circular diffraction patterns. For an aspect ratio of unity, the relationship between $\Delta\theta$ and $\Delta\rho$ can be written as

$$\Delta\rho = \frac{b}{2\arctan\left(\frac{b}{2\sqrt{R^2-\rho^2}}\right)}\Delta\theta, \tag{1}$$

where b is the width of a Kikuchi band, R is the radius of the circular pattern, and ρ is the coordinate of the peak in Hough space (Fig. 3). The latter is bounded between $-R$ and R. Given the position of the EBSD camera with respect to the sample (pattern center and detector distance), the accelerating voltage, and the phases present in the sample, the theoretic range of b can be determined. For example, the width of the 10 most intense Kikuchi bands of a pure copper sample varies between 16 and 67 pixel (calculated from 100 random orientations at 20 keV with a diffraction pattern of 672 × 512 pixels). With these boundaries, an approximation of the proportionality constant between $\Delta\theta$ and $\Delta\rho$ can be calculated by numerically integrating equation (1) between the width ($b_0 = 16$ pixels to $b_1 = 67$ pixels) and ρ ($\rho_0 = -256$ pixels to $\rho_1 = 256$ pixels) ranges:

$$\Delta\rho = \frac{1}{2(\rho_1-\rho_0)(b_1-b_0)} \times \left(\int_{b_0}^{b_1}\int_{\rho_0}^{\rho_1} \frac{b}{2\arctan\left(\frac{b}{2\sqrt{R^2-\rho^2}}\right)} \mathrm{d}b\,\mathrm{d}\rho\right)\Delta\theta. \tag{2}$$

Equation (2) ensures that the aspect ratio will be close to unity for a large portion of the Hough space, independent of the selected $\Delta\theta$ resolution and dimensions of the diffraction patterns.

As stipulated by Krieger Lassen (1994), the height of a peak (h) is directly proportional to the width of its Kikuchi band (b).

$$h = \frac{b}{\Delta\rho}. \tag{3}$$

The size of the convolution mask therefore can be selected based on the average theoretical width of the Kikuchi bands, as calculated to solve the integral. In the case of the copper sample, the average width of the bands is 30.5 pixels and, for a $\Delta\theta$ of 1°/pixels, the calculated $\Delta\rho$ from the integral is 3.76 pixels/pixels, giving a peak height of 8 pixels. A convolution mask of 9 × 9 pixels would be appropriate.

To detect peaks in the Hough space, two algorithms are currently implemented in EBSD-Image. The first is an adaptation of the top hat algorithm presented by Gonzalez and Woods (2007). The average value between the min error (Kittler & Illingworth, 1986) and entropy (Kapur et al., 1985) thresholding methods is used after the top hat to create the binary image. The second peak detection algorithm uses the statistical distribution of the Hough space to threshold peaks from the background. It utilizes the fact that peaks have an intensity greater than the average intensity by some multiple of the standard deviation, as defined by the user.

Three peak positioning methods are currently available in EBSD-Image: centroid, center of mass, and maximum position. From the binary image of detected peaks, the first method finds the geometric centroid of each peak and takes this value as the position of the peak. The second method was proposed by Krieger Lassen (1998): the center of mass is calculated using the intensity of the pixels. Finally, the third method finds the position of the pixel with the maximum value inside a given peak. For each of these methods, the intensity of a peak is taken as the value of the closest pixel to its position.

File Formats

EBSD-Image introduces two file formats to facilitate the manipulation of large numbers of diffraction patterns and processing of the resulting maps. Far from being proprietary to EBSD-Image, they are designed to be simple and easily implementable by other software.

In commercial software, diffraction patterns are saved as individual files.[a] Even with 50,000+ images, the space required to save all EBSPs is no longer a problem with current hard drives. However, the number of files stored inside a single folder is a challenge for the operating system. Browsing a folder containing this amount of files is slow and inefficient. This problem becomes apparent when one attempts to move or copy those folders. On an Intel Xeon 3 GHz computer (3 GB of RAM, 7,200 rpm SATA hard drive) with the Microsoft Windows XP operating system, it takes 1 min to browse a folder containing 50,298 images. The transfer of these files to a portable magnetic hard drive via a USB 2.0 connection takes just over 18 min. To remedy to this situation, we propose a simple file format to store and access all EBSPs: the stream maps or SMP file. Thousands of small image files are replaced by a single, large SMP file. Images are saved in sequence from the upper left corner of a map down to the lower right corner. On the same computer described above, the inclusion of 50,298 images into a SMP file takes approximately 2 min and 30 s. The real advantage comes when transferring the SMP file to another media format: it took 1 min to copy the SMP file to the same portable hard drive.

To have a more open and flexible file format, EBSD-Image uses a different scheme to store its results. All results from an experiment can be saved in maps/images: one map to identify the location of each phase, one map for each of the three Euler angles, one map per quality metric, etc. These different images are stored inside a ZIP file with a specific structure dubbed EBSD multimap (short for multiple map). There are no restrictions on the type or number of maps in a multimap. Apart from the images, the ZIP file contains an XML file to store metadata (parameters and properties) related to an EBSD acquisition.

[a]The common file formats are JPG, BMP, or TIFF. However, the possibility of saving diffraction patterns as images during an acquisition is not available in all EBSD software.

Processing of Large Dataset

With the advent of faster EBSD cameras, the size and/or the quantity of EBSD acquisitions and consequently the number of diffraction patterns acquired will only increase in coming years (Brough & Humphreys, 2010; Schwarzer & Hjelen, 2010). EBSD-Image has been developed with the capability to process and analyze large datasets. Three utilities are currently available: (1) the aforementioned SMP file, (2) the stitching of mappings and combination of corresponding diffraction patterns, and (3) the use of a distributed computing grid.

One common strategy used to cover a large area of a sample is to acquire several mappings and later stitch them into one single mapping. In the case of an EBSD dataset, stitching involves the combination of the information contained in each mapping (orientation, quality metrics, etc.) as well as the diffraction patterns. Commercial software provides tools to stitch different mappings together, but the relation between the pixel positions and the EBSP image files is lost. Hence, a routine was written in EBSD-Image to simultaneously combine different EBSD multimaps and SMP files. Those maps can then be reprocessed.

The EBSD analysis requires computer-intensive calculations, such as the Hough transform, to be performed on tens of thousands of images. If one wants to use more elaborate but perhaps slower algorithms to analyze these diffraction patterns, processing large quantities of data can easily become a problem, or at the very least a limitation. Since each diffraction pattern is completely independent from the others, the same set of algorithms can be independently applied on each one and the results combined at the end. New commercial software with "fast" cameras use multiple processors during the acquisition. The distributed interface of EBSD-Image offers the same capability but on more than one computer, and it is detached from the graphical interface. There is no limitation on how many processors can be used. This allows the use of distributed computing on a grid or cluster of computers.

Materials and Methods

Sample Preparation

This study evaluates the deformation behavior of two pure metals: copper and iron, which have different crystal structures and slip systems. As specified by the supplier, their purity is at least 99.99%. We selected samples with large grains to minimize the effects of grain boundaries. The samples were deformed by 220 grit SiC grinding paper. This design of experiment is similar to that of Samuels (2003), who used light optical and transmission electron microscopy to study the deformation of several grinding media.

The samples had to be carefully prepared to prevent further deformation. From the stock block, two samples of each metal were cut out using the proper abrasive cutting wheel and sectioned as small cubes. Having right angles between the faces of the sample was important for the later steps. One sample was deformed using the grinding paper

while the other was used as a control. The samples were mounted in Bakelite and polished up to colloidal silica to remove any deformation induced during sectioning. The deformed samples were ground for 1.5 min on 220 grit SiC grinding paper with a force of 20 N and polishing disk rotation speed of 300 rpm in the complementary direction with respect to the polishing head. All samples were then unmounted from the Bakelite. The deformed surface was nickel plated (3–5 μm thick layer) to protect it from subsequent operations of the preparation procedure. The samples were then mounted sideways in Bakelite: in other words, the deformed surface was now perpendicular to the polishing surface of the mount. The samples were polished up to colloidal silica. All steps were performed on automated polishing equipment to eliminate any human intervention. No chemical attack or electro-polishing techniques were used.

Acquisition Parameters

Diffraction patterns were acquired using a Hitachi S-4700 (cold field emitter) microscope equipped with a NordlysS and the HKL Channel 5 software (Oxford Instruments plc, Tubney Woods, Abingdon, Oxfordshire, UK). An accelerating voltage of 20 keV, binning of 8×8 (168×128 pixels), and 10 ms dwell time were used for the mappings. Diffraction patterns were saved without any compression. The samples were aligned to position the deformed surface perpendicular to the tilt axis to ensure the best resolution along the deformation profile. Diffraction patterns were processed on the computing cluster of the Hydro-Québec Research Institute (AMD Opteron 2218 processors, Linux Centos 4.4 operating system, and Sun Grid Engine nodes management system).

Calculation of Quality Metrics

One of the first applications of EBSD-Image was to determine which quality metrics are suitable to detect variation in deformation level. Several quality metrics are described in the literature; some of these were successfully used to study deformed samples, while others did not give any deformation information. Based on the concepts used in the elaboration of these quality metrics, new ones have been defined and measured using EBSD-Image. The flexible structure of EBSD-Image facilitates the implementation and evaluation of any quality metric.

We used a systematic approach to define new quality metrics. The quality of a diffraction pattern can be directly estimated from the pattern itself or calculated from the intensity of the peaks in Hough space. From an implementation point of view, these two categories use different information to calculate quality metrics; one is based on the diffraction pattern and the other on the detected peaks and their intensities. The intermediate step between these two types of information is the Hough transform. Logically, the result of the Hough transform could provide a useful evaluation of the diffraction quality. Different mathematical and statistical operations can be performed on these sources of information to obtain a value expressing the diffraction quality. For instance, Tao (2003) used the average, standard deviation and Shannon's entropy of the diffraction patterns. Other simple operations are the range (the difference between the maximum and the minimum value of a dataset), the sum (the addition of all the values of a dataset), or the number of items in the dataset.

Table 1. Summary of the Quality Metrics That Will Be Studied Based on Their Ability to Assess the Level of Deformation.

	Pattern	Hough	Detected Peaks
Average	?	?	?
Standard deviation	?	?	?
Entropy	?	?	N/A
Range	?	?	?
Sum	?	?	?
Count	N/A	N/A	?
Others	Fourier transform Signal-to-noise	—	Band contrast Band slope Pattern quality Local difference

By combining the three sources of information (diffraction pattern, Hough space, and detected peaks) with these operations, we obtain a table of 18 possible quality metrics (Table 1). Taking the average operation as an example, a quality metric can be calculated from the mean of the pixels in the diffraction pattern, the pixels of the Hough space, or the intensities of the detected peaks. Three quality metrics, however, can be removed from the list: the operation evaluating the number of items in the data does not apply to the diffraction pattern and Hough space because the number of items, i.e., the number of pixels, is constant. It is only valid for the detected peaks. Also, the entropy operation is not applicable to the intensities of the detected peaks as they do not constitute a probabilistic distribution.

Apart from these 15, three additional quality metrics found in the literature were implemented: one based on the Fourier transform proposed by Krieger Lassen (1994), the signal-to-noise ratio calculated using the cross correlation between odd and even rows of a given image (Frank & Al-Ali, 1975), and the pattern quality reportedly used by the INCA Crystal system (Oxford Instruments plc). We also introduced four other quality metrics, grouped under "local difference" in Table 1. They are based on the difference between the maximum and minimum value inside each detected peak, i.e., the range operation is applied on every detected peak.

Removal of Artifacts

As mentioned by Wu et al. (2005), grain boundaries and surface defects are regions in a mapping where diffraction patterns have a lower quality. To eliminate the effect of these elements on the calculation of deformation depth, they are excluded using a mask. Surface defects such as scratches and debris are easily identifiable and can be manually removed.

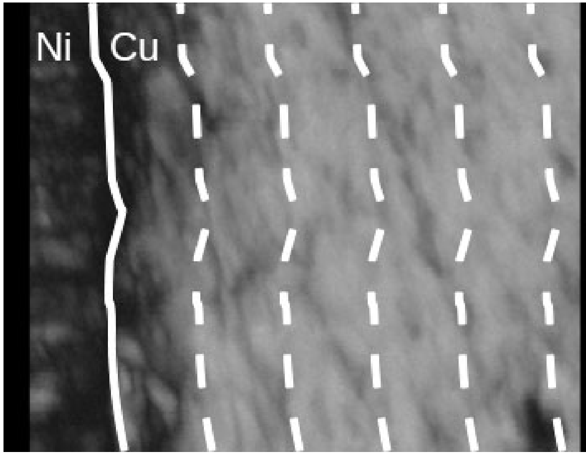

Figure 5. Schematic representation of the slices used to calculate the deformation profile. The solid line represents the interface between the copper sample and the nickel plating. The dashed lines delineate the slices.

As for grain boundaries, a two-pixels-wide region along each grain boundary is added to the mask. The detection of grain boundaries was performed with the HKL Channel 5 software using a 5° misorientation criteria. This information was then processed using EBSD-Image to create the two-pixels-wide region.

Deformation Depth

For all samples in this study, the level of deformation should be at its maximum near the deformed surface. The values in the quality maps are expected to increase as a function of the distance from the deformed surface up to the undeformed region. This variation should increase monotonically as the samples were uniformly deformed.

To obtain such a profile, the following steps were performed on each map of the different samples. The first step is to precisely determine the coordinates of the deformed surface. Because of the electroplated layer of nickel, the latter does not correspond to the edge of the sample. A zigzag line made of several points is used to delineate the surface. The second step is to segment the map into successive vertical slices starting from the deformed surface. All of the slices have the same thickness and therefore the same number of pixels. Figure 5 schematically shows five slices of a given map. The solid line from the left corresponds to the deformed surface. In reality, about twenty-five 10-pixels-wide vertical slices are taken per map. The final step is to calculate the mean value of the pixels inside each slice. This value is plotted as a function of the distance of the slice from the deformed surface. The greater the number of pixels in a slice, the better the statistics of the profile. The deformation depth can be defined as the distance from the deformed surface, where the quality reaches 90% of the plateau. In other words, the depth extends from the deformed surface up to a region with a deformation level of 10%.

By comparing different deformation profiles, the quality metrics can be evaluated based on their ability to assess the level of deformation. This study did not look at the influence of experimental conditions on the quality metrics. Furthermore, the same Hough transform resolution (1°/pixel) as well as the same algorithms for peak detection (standard deviation after applying a 9 × 9 butterfly mask) and peak positioning (center of mass) were used for each quality metric. It is certainly possible that the algorithms used could influence the results obtained from the quality metrics. Our comparison is therefore qualitative and closely linked with one of the scopes of this application: to measure deformation depth induced during grinding.

Results and Discussion

Benchmarking

Simulated diffraction patterns were used to benchmark the peak detection and positioning algorithms implemented in EBSD-Image. Simulations were generated using the kinematic diffraction model for a given set of experimental conditions (accelerating voltage, calibration of the camera, crystalline structure, and orientation). Benchmarking therefore can be used to compare the theoretical positions of the most intense Kikuchi bands with those measured after different peak detection or positioning algorithms. Other advantages of using simulated diffraction patterns are that they are free of any lattice distortion, independent of acquisition parameters (integration time, gain, background correction, etc.), and allow a large range of orientations to be explored. To test the ability of the detection and positioning algorithms to deal with high and low quality diffraction patterns, noise and smoothing filters were independently applied on each diffraction pattern. More precisely, the noise level in the pattern was calculated from the equation used by Cizmar et al. (2008) on simulated scanning electron microscope (SEM) images. It consists of the combination of Poisson noise, representing the noise from the electron interactions statistics, and Gaussian noise, attributed to the camera's electronics:

$$C_2 = C_1 + (\sigma + P\sqrt{C_1})Z, \tag{4}$$

where C_1 is the original intensity of a pixel, C_2 the final intensity, σ the standard deviation of Gaussian noise, P the amplitude of Poisson noise, and Z a random number normally distributed. The electronics noise is constant for a given EBSD system and set of experimental conditions: we assume a standard deviation of 25 for the Gaussian noise. The amplitude of the Poisson noise was varied between 0 and 64 to simulate an increase in the noise level. The smoothing filter replaces the intensity of a pixel by the average intensity of its neighbors. It has the effect of blurring the Kikuchi bands. As the number neighbors used in the calculations is increased, the smoothing and blurring of the image are also increased. For this study, the smoothing level was increased up to a kernel of 31 × 31.

In the following results, the same set of 10 randomly oriented diffraction patterns was used. They were calculated for a copper crystal observed at 20 keV. The use of different

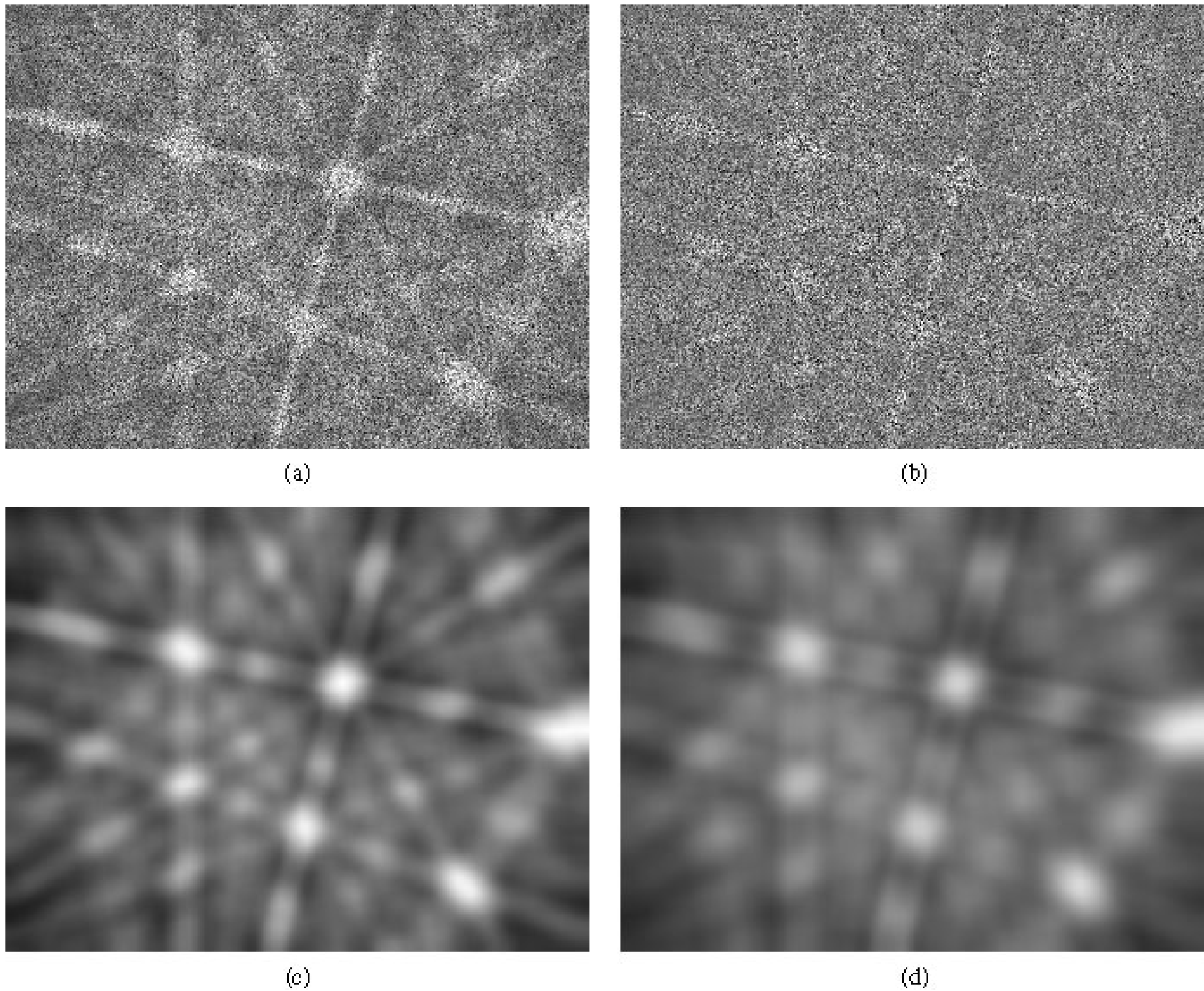

Figure 6. Examples of simulated diffraction patterns for a copper crystal at 20 keV after (**a**,**b**) a noise filter and (**c**,**d**) a smoothing filter were applied. The standard deviation for the Gaussian noise is constant at 25 in (**a**,**b**) whereas the amplitude of the Poisson noise is (**a**) 8 and (**b**) 24. The kernel size of the smoothing filter is (**c**) 15 × 15 and (**d**) 23 × 23. The same crystal orientation is shown in all four diffraction patterns.

orientations is important as the reflectors change from one diffraction pattern to another. Figure 6 shows an example of four simulated diffraction patterns.

A good peak detection algorithm should be able to detect as many peaks as possible in the Hough transform, without reporting peaks that do not correspond to a Kikuchi band (false positive). The benchmarking of two peak detection algorithms in EBSD-Image (top hat and standard deviation) as well as the detection obtained using two commercial EBSD software programs (A & B) was done by evaluating the detection of the 10 most intense peaks in Hough space. We arbitrarily defined a peak to be correctly detected if it is located within a 5 pixel radius of the theoretical position of its Kikuchi band.[b] For the peak detection algorithms in EBSD-Image and software A, a $\Delta\theta$ resolution of 1°/pixel was used for the Hough transform and a 9 × 9 butterfly mask was applied. The positions of the peaks were directly exported. For software B, a Hough resolution of 60 (suggested for accurate detection in the user manual) and the "band centers" detection method were selected. The positions of the peaks were back-calculated from the "band detection" image. Figure 7 shows the number of correctly detected bands for the four algorithms as a function of (a) the amplitude of the Poisson noise and (b) the kernel size of the smoothing filter. The value of each point corresponds to the average of the 10 randomly oriented diffraction patterns, whereas the error bars are the 95% confidence interval.

Benchmarking shows that the two algorithms proposed in EBSD-Image are comparable to the ones used in commercial software. All algorithms follow the same trend as the level of deterioration of the diffraction patterns is increased. With the selected experimental parameters, software A does not perform as well on noisy diffraction patterns. The top hat algorithm has more difficulty in detecting the peaks. Further investigation revealed that the butterfly mask may

[b]With the resolution used, it is equivalent to a 5° difference in the θ direction and 9 pixel difference in the ρ direction of the Hough space.

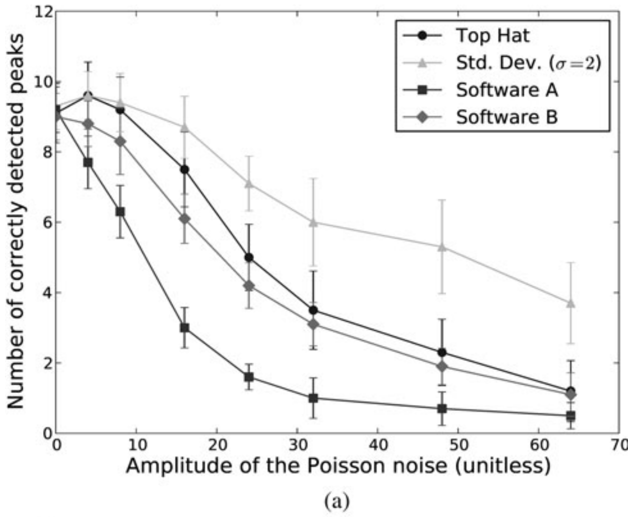

(a)

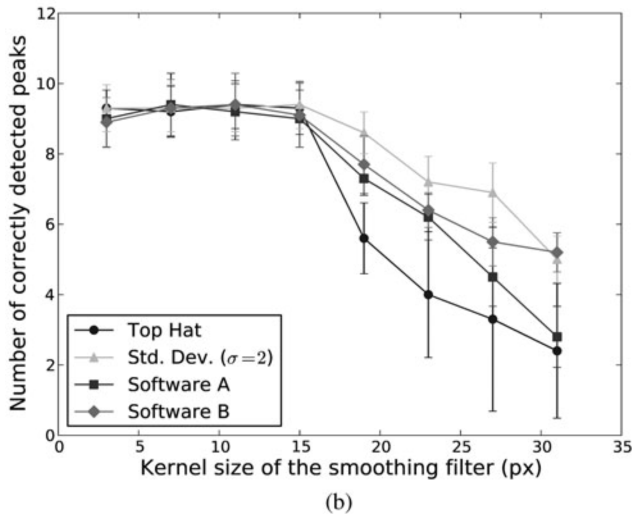

(b)

Figure 7. Number of correctly detected bands by different peak detection algorithms as a function of (**a**) the amplitude of the Poisson noise and (**b**) the kernel size of the smoothing filter.

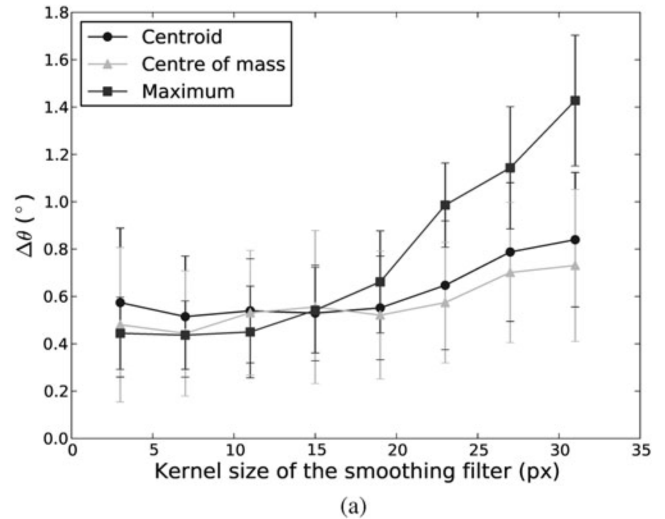

(a)

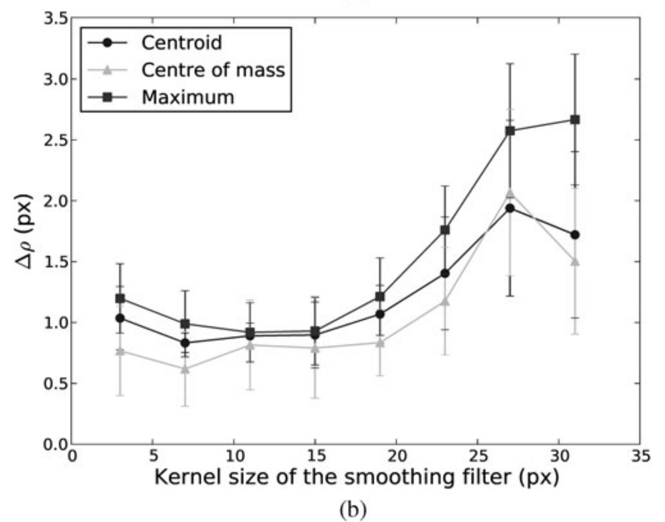

(b)

Figure 8. Accuracy of the peak positioning algorithms of EBSD-Image in the (**a**) θ and (**b**) ρ directions of the Hough space as a function of the kernel size of the smoothing filter.

have an adverse effect on this algorithm. If no butterfly mask is applied on the Hough space, the top hat algorithm correctly detected as many peaks as the standard deviation algorithm.

Benchmarking of peak positioning was performed in a similar manner on the three aforementioned algorithms of EBSD-Image (centroid, center of mass, and maximum position). The comparison could not be made with commercial software due to the loss of precision in the conversion of data. The accuracy of the identification procedure was evaluated based on the distance in θ and ρ between the theoretical and identified position of the peaks. The results are shown in Figure 8 as a function of the kernel size of the smoothing filter. Overall the three identification algorithms give a similar accuracy on the position of peaks. The centroid and center of mass may be slightly better than the maximum position algorithm. Even for highly blurred Kikuchi bands, the precision of correctly detected peaks is within 3 pixels in the θ and ρ directions of the Hough space (3° angular mismatch and 5 pixel shift). The same accuracy is found on noisy patterns. Consequently, the three algorithms are able to properly position the center of the Kikuchi bands.

Deformation

The profiles of the iron and copper control (undeformed) samples show no apparent deformation. Figure 9 compares the profile of the control and deformed copper samples. The values are calculated from the quality metric based on the Fourier transform. There are small variations in the profile of the control sample, which could be related to surface cleanliness and polishing relief. These effects combined with the difficulty of properly identifying the edge of the sample (after the nickel plated layer) may pose a challenge in the evaluation of smaller deformation depths. For instance, it may not be possible to reliably determine the deformation induced by finer grit paper or by diamond polishing with this method of analysis.

Different deformation depths are obtained depending on the quality metric used, even if we exclude the quality metrics that did not evaluate deformation. Figure 10 shows

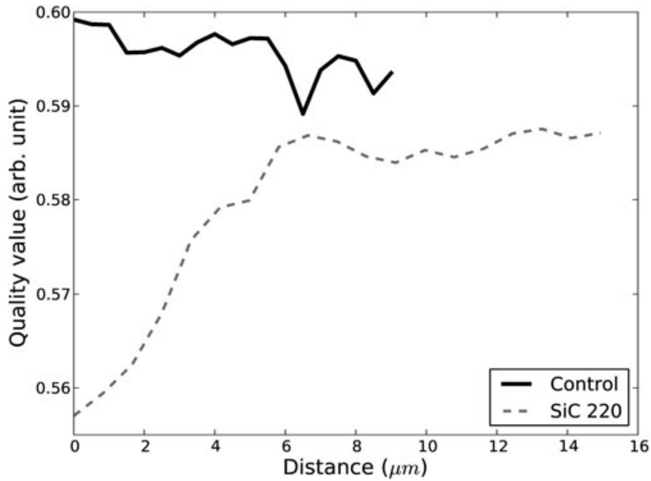

Figure 9. Comparison between the deformation profile of the control and deformed copper samples. The quality metric based on the Fourier transform is shown.

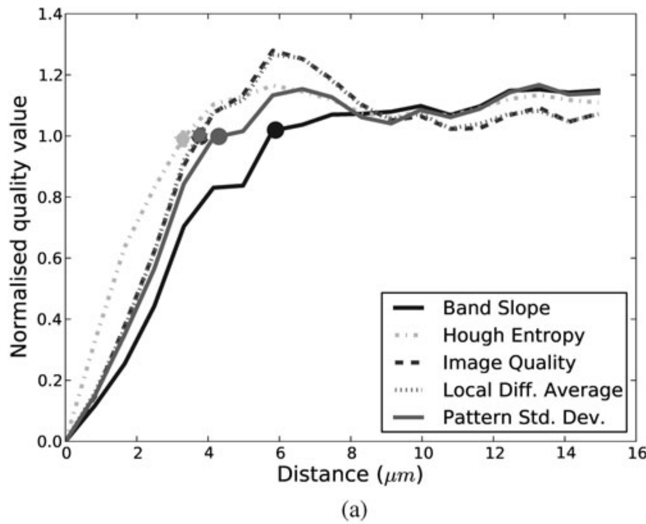

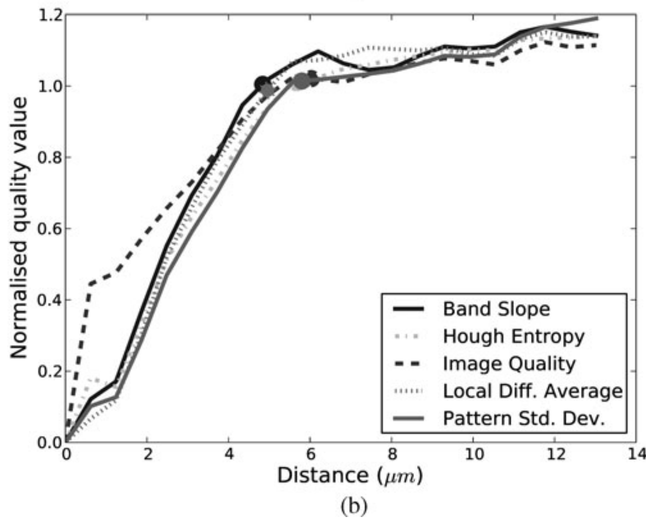

Figure 10. Deformation profiles obtained by five quality metrics on (**a**) the copper and (**b**) iron samples. The circle markers indicate the deformation depth.

Table 2. Evaluation of Quality Metrics Based on Their Ability to Assess the Level of Deformation.

	Pattern	Hough	Detected Peaks
Average	Bad	Bad	Good
Standard deviation	Good	Good	Fair
Entropy	Good	Good	N/A
Range	Good	Good	Fair
Sum	Bad	Bad	Good
Count	N/A	N/A	Fair
Others	Fourier transform Signal-to-noise	—	Band contrast Band slope Pattern quality Local difference

the deformation profiles obtained using the band slope, Hough entropy, image quality, average local difference, and pattern standard deviation quality metrics for the copper (Fig. 10a) and iron (Fig. 10b) samples. The deformation depth found ranges between 3 and 7 μm for the copper sample and between 4 and 6 μm for the iron sample. The variation in the deformation depth indicates that some quality metrics may underestimate the deformation while others may overestimate it. These measurements are comparable with those obtained by Samuels (2003) on a 30% Zn brass. By visual inspection of the sample after etching, he measured a significant deformation depth of 7.5 μm, but he also observed signs of the deformation up to 77 μm below the surface. Regions of small localized deformation may be difficult to quantitatively assess using quality metrics due to their dependence on crystallographic orientation and other defects such as grain boundaries. Techniques based on local misorientation (Brewer et al., 2009) and small variations in the diffraction patterns (Wilkinson et al., 2005) would be more suitable to locate small strain levels.

Evaluation of Quality Metrics

We shall define three categories of quality metrics based on their ability to evaluate deformation. A good quality metric must meet the following requirements for all iron and copper samples: (1) a deformation profile showing monotonic increase as a function of depth and (2) a relatively similar deformation depth to other quality metrics for a given sample. A fair quality metric would comply with some of these requirements or only for some samples, whereas a bad quality metric does not meet any requirements.

Table 2 summarizes the evaluation of the quality metrics. The comparison of mappings from quality metrics calculated from the diffraction patterns or the Hough spaces reveals some similarity between these two sources of information. This can be explained by the fact that the intensities in the Hough space are derived from those in the diffraction pattern. On the other hand, the contrast in the Hough range mapping is more enhanced than that of the pattern range mapping due to the concentration of high intensities in the Hough peaks. Our results for the average metric agree with

Wright and Nowell's (2006) observations that this metric is relatively unaffected by deformation. The same trend is observed using the sum of intensities. The standard deviation and range are able to measure the increase in contrast as more intense Kikuchi bands emerge from deformed patterns. Shannon's entropy gives a good measure of the deformation; however, further measurements are required to fully understand how the estimation of the compressibility of an image and the level of deformation are related.

The quality metrics evaluated using the intensities of detected peaks are inherently dependent on the number of peaks detected. For this reason, the operations (average, standard deviation, etc.) were performed on the three to seven most intense peaks as well as on all detected peaks. We found that the number of peaks used in the calculations has little influence on the average but leads to a large variation of the deformation depth for the standard deviation and the range (50% difference). The sum is more affected than the average but less than the standard deviation and the range. This behavior could be explained by the presence of false peaks in the deformed region that would increase the variability in the intensity of the peaks. With low intensity, these false peaks have a minor effect on the average and the sum. The number of detected peaks is successful in measuring the deformation depth on the iron sample only. Of all the quality metrics tested, the latter would be most affected by the presence of false peaks. Nevertheless, it is difficult to explain the different behavior between copper and iron samples. From the grain maps, the copper samples have more recrystallized grains than the iron ones near the deformed surface. The presence of these grains may increase the average number of detected peaks and disrupt the deformation profile.

Other good quality metrics are the band contrast (calculated by HKL Channel 5), the band slope (calculated by HKL Channel 5), and the one calculated from the Fourier transform. The pattern quality (as in Oxford INCA) gives a fair response to deformation because it could not correctly evaluate the deformation depth for all samples: its values were found to vary and decrease in the undeformed region. The signal-to-noise ratio was not able to properly evaluate the deformation: this quality metric was inversely proportional to the deformation depth, having its maximum value at the deformed surface.

The quality metrics based on the local difference within the detected peaks were also able to detect the level of deformation. It was found that the average, standard deviation, and maximum of the local difference values give similar deformation depths and distributions. The minimum intensity difference does not seem to carry any deformation information.

The set of simulated diffraction patterns used for the benchmarking of algorithms can also help understand how different quality metrics evaluate the level of deformation in a sample. Instead of the number of detected peaks or the accuracy, the quality metrics are calculated from diffraction patterns at different levels of deterioration. As previously discussed, distortion in the lattice at the level of the interaction volume leads to blurring of the edges of the Kikuchi bands. The smoothing filter was used to mimic this effect. The measurements were normalized by the quality value of the initial simulated pattern without any deterioration. Figure 11 illustrates the results for five quality metrics: three identified as good evaluators of deformation (pattern entropy, maximum local difference, and peaks average), one which had a fair response (peaks standard deviation), and one found to be insensitive to deformation (Hough average). The good quality metrics show a decrease in their quality as the blurriness of the Kikuchi bands is increased. The fact that the maximum local difference has a large change in comparison with the pattern entropy and the peaks' average does not imply that the former is more sensitive to deformation than the others. The curves show the relative variation for each quality metric, not the absolute change because the effective theoretical range of the quality metrics is unknown. The peaks' standard deviation has a similar trend but a larger variability than the good quality metrics, which could explain its fair response to deformation. As expected, the Hough average is constant as it is not affected by the sharpness of the diffraction patterns. The influence of the orientation on the quality metrics is evaluated by the error bars. The simulations suggest that the pattern entropy is less influenced by orientation than the maximum local difference and the peaks' average. It is not possible, however, to experimentally validate this observation with the samples used in this study.

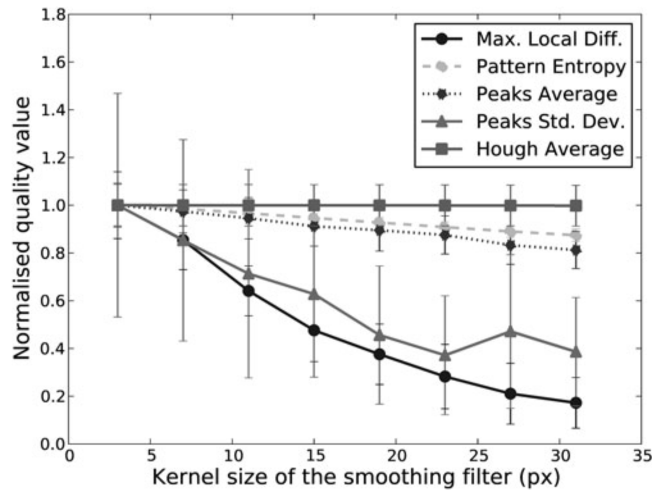

Figure 11. Variation of the quality metrics as a function of the kernel size of the smoothing filter.

Conclusion

EBSD-Image is an open source program for processing Kikuchi patterns. It allows the user to add any type of processing algorithm to analyze diffraction patterns acquired during a mapping. In the current version, different quality metrics can be computed. They are as valuable as the different electron signals now found in modern SEMs,

namely secondary (upper or lower detector) and backscatter electrons detector (low and high angle) because they can reveal different properties of the microstructure. Some are implemented in commercial EBSD acquisition software, but the implementation of new metrics within these software packages is not possible, leaving users to design their own system. EBSD-Image provides an alternative solution to this problem. Its flexible analytical structure is designed to facilitate the implementation of recognized algorithms and the development of new ones. Fourteen out of 24 quality metrics were found to properly evaluate the level of deformation inside copper and iron samples mechanically deformed by a 220 grit SiC grinding paper. Benchmarking using simulated diffraction patterns validated the algorithms used in EBSD-Image, which were comparable to those in commercial software. However, as an open research and development platform, EBSD-Image offers the possibility to develop better and more appropriate algorithms for the EBSD community.

Acknowledgments

Hydro-Québec is greatly acknowledged for providing access to their facility. The authors would also like to acknowledge the contribution of H. Demers in the functional testing of the software on the MacOS X operating system, F. Bridier and Prof. Bocher of École de technologie supérieure for their kindness in letting us use their microscope for preliminary work leading to this article, Benoît Morin of Hydro-Québec for his expertise and support on operating the computer grid, and G. Vander Voort for his advice and expertise throughout this project.

References

Brewer, L.N., Field, D.P. & Merriman, C.C. (2009). Mapping and assessing plastic deformation using EBSD. In *Electron Backscatter Diffraction in Materials Science*, Schwartz, A.J., Kumar, M., Adams, B.L. & Field, D.P. (Eds.), pp. 251–262. New York: Springer.

Brough, I. & Humphreys, F.J. (2010). Evaluation and application of a fast EBSD detector. *Mater Sci Technol* **26**, 636–639.

Cizmar, P., Vladár, A.E., Ming, B. & Postek, M.T. (2008). Simulated SEM images for resolution measurement. *Scanning* **30**, 381–391.

Frank, J. & Al-Ali, L. (1975). Signal-to-noise ratio of electron micrographs obtained by cross-correlation. *Nature* **256**, 376–379.

Gonzalez, R.C. & Woods, R.E. (2007). *Digital Image Processing*. 3rd ed. Upper Saddle River, NJ: Prentice Hall.

Hielscher, H. & Schaeben, H. (2008). A novel pole figure inversion method: Specification of the MTEX algorithm. *J Appl Crystallog* **41**, 1024–1037.

Hovington, P., Pinard, P.T., Lagacé, M., Rodrigue, L., Gauvin, R. & Trudeau, M.L. (2009). Towards a more comprehensive microstructural analysis of Zr-2.5Nb pressure tubing using image analysis and electron backscattered diffraction (EBSD). *J Nucl Mater* **393**, 162–174.

Humphreys, F.J. (2004). Characterisation of fine-scale microstructures by electron backscatter diffraction (EBSD). *Scripta Mater* **51**, 771–776.

Kapur, J.N., Sahoo, P.K. & Wong, A.K.C. (1985). A new method for gray level picture thresholding using the entropy of the histogram. *Comput Vis Graphics Image Process* **29**, 273–285.

Keller, R.R., Roshko, A., Geiss, R.H., Bertness, K.A. & Quinn, T.P. (2004). EBSD measurement of strains in GaAs due to oxidation of buried AlGaAs layers. *Microelec Eng* **75**, 96–102.

Kittler, J. & Illingworth, J. (1986). Minimum error thresholding. *Pattern Recogn* **19**, 41–47.

Krieger Lassen, N.C. (1994). Automated determination of crystal orientations from electron backscattering patterns. PhD thesis, The Technical University of Denmark.

Krieger Lassen, N.C. (1998). Automatic high-precision measurements of the location and width of Kikuchi bands in electron backscatter diffraction patterns. *J Microsc* **190**, 375–391.

Petrov, R., Kestens, L., Wasilkowska, A. & Houbaert, Y. (2007). Microstructure and texture of a lightly deformed TRIP-assisted steel characterized by means of the EBSD technique. *Mater Sci Eng A* **447**, 285–297.

Ryde, L. (2006). Application of EBSD to analysis of microstructure in commercial steels. *Mater Sci Technol* **22**, 1297–1306.

Samuels, L.E. (2003). *Metallographic Polishing*, 4th ed. Materials Park, OH: ASM International.

Schwarzer, R.A. & Hjelen, J. (2010). Orientation microscopy with fast EBSD. *Mater Sci Technol* **26**, 646–649.

Tao, X. (2003). An EBSD study on mapping of small orientation differences in lattice mismatched heterostructures. PhD thesis, Lehigh University.

Tao, X. & Eades, A. (2005). Errors, artifacts, and improvements in EBSD processing and mapping. *Microsc Microanal* **11**, 79–97.

Wilkinson, A.K. & Dingley, D.J. (1991). Quantitative deformation studies using electron backscatter patterns. *Acta Metall Mater* **39**, 3047–3055.

Wilkinson, A.J., Meaden, G. & Dingley, D.J. (2005). High-resolution elastic strain measurement from electron backscatter diffraction patterns: New levels of sensitivity. *Ultramicroscopy* **106**, 307–313.

Wright, S.I. (1992). Individual lattice orientation measurements development and application of a fully automatic technique. PhD thesis, Yale University.

Wright, S.I. & Nowell, M.M. (2006). EBSD image quality mapping. *Microsc Microanal* **12**, 72–84.

Wu, J., Wray, P.J., Garcia, C.I., Hua, M. & Deardo, A.J. (2005). Image quality analysis: A new method of characterizing microstructures. *ISIJ Int* **45**, 254–262.